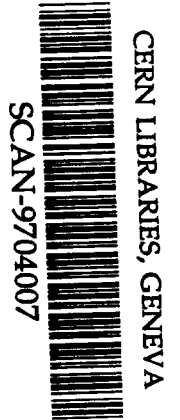JA

ISTITUTO NAZIONALE DI FISICA NUCLEARE

Sezione di Trieste

SW9714

THE COSMIC RAY ANTIPROTON FLUX BETWEEN 0.62 AND 3.19 GeV MEASURED NEAR SOLAR MINIMUM

WIZARD Collaboration

The cosmic ray antiproton flux between 0.62 and 3.19 GeV measured near solar minimum activity

M. Boezio[1], P. Carlson, T. Francke, N. Weber

Royal Institute of Technology (KTH), S-104 05 Stockholm, Sweden

M. Suffert

Centre des Recherches Nucléaires, BP20, F-67037 Strasbourg-Cedex, France

M. Hof, W. Menn and M. Simon

Universität Siegen, 57068 Siegen, Germany

S. A. Stephens

Tata Institute of Fundamental Research, Bombay 400 005, India

R. Bellotti, F. Cafagna, M. Castellano, M. Circella, G. De Cataldo, C. De Marzo,

N. Giglietto and P. Spinelli

Dipartimento di Fisica dell'Università and Sezione INFN di Bari, Via Amendola 173,

I-70126 Bari, Italy

M. Bocciolini, P. Papini, A. Perego, S. Piccardi and P. Spillantini

Dipartimento di Fisica dell'Università and Sezione INFN di Firenze, Largo Enrico Fermi 2,

I-50125 Firenze, Italy

G. Basini and M. Ricci

Laboratori Nazionali INFN, Via Enrico Fermi 40, CP 13, I-00044 Frascati, Italy

A. Codino, N. Finetti and C. Grimani

Dipartimento di Fisica dell'Università and Sezione INFN di Perugia, Via Pascoli, I-06100

Perugia, Italy

M. Candusso, M. Casolino, M.P. De Pascale, A. Morselli, P. Picozza and R. Sparvoli

Dipartimento di Fisica dell'Università and Sezione INFN di Roma, Tor Vergata, Via della

Ricerca Scientifica 1, I-00133 Roma, Italy

G. Barbiellini, U. Bravar, P. Schiavon, A. Vacchi and N. Zampa

Dipartimento di Fisica dell'Università and Sezione INFN di Trieste, Via A. Valerio 2,

I-34147 Trieste, Italy

J.W. Mitchell, J.F. Ormes and R.E. Streitmatter

Code 661, NASA/Goddard Space Flight Center, Greenbelt, MD 20771

and

R. L. Golden[2] and S.J. Stochaj

Box 3-PAL, New Mexico State University, Las Cruces, NM 88003

---

[1]Also at Sezione INFN di di Trieste, Via A. Valerio 2, I-34147 Trieste, Italy

[2]Deceased

ABSTRACT

We report on the absolute antiproton flux and the antiproton to proton ratio in the energy range 0.62 to 3.19 GeV at the top of the atmosphere, measured by the balloon-borne experiment CAPRICE flown from Lynn Lake, Manitoba, Canada, on August 8-9, 1994. The experiment used the NMSU-WiZard/CAPRICE balloon-borne magnet spectrometer equipped with a solid radiator Ring Imaging CHerenkov (RICH) detector and a silicon-tungsten calorimeter for particle identification. This is the first time a RICH is used together with an imaging calorimeter in a balloon experiment, and it allows antiprotons to be clearly identified over the rigidity range 1.2 to 4 GV/c. Nine antiprotons were identified in the energy range from 0.62 to 3.19 GeV at the top of the atmosphere. The data were collected over 18 hours at a mean residual atmosphere of 3.9 g/cm^2. The absolute antiproton flux is consistent with a pure secondary production of antiprotons during the propagation of cosmic rays in the Galaxy.

1. Introduction

Antimatter in the form of antiprotons and positrons is a natural component of the cosmic rays being produced in interaction between cosmic ray nuclei and the interstellar medium. Detailed knowledge of the antimatter flux is important in order to fully understand the origin, production and the transport mechanisms of cosmic rays in our galaxy. The first experimental evidence for the presence of antiprotons in the cosmic rays was reported by Golden et al. (1979) and was subsequently followed by other experiments (Bogomolov et al. 1979, Buffington et al. 1981) which all report a ratio of the flux of antiprotons to protons above that expected for a purely secondary production process.

Subsequently several ideas were suggested to explain the antiproton excess: antimatter reaching our galaxy from antimatter galaxies in a baryon-antibaryon symmetric universe (e.g. Stecker et al. 1981, Stecker & Wolfendale 1984), antimatter production by dark matter annihilation and antimatter production by the evaporation of primordial mini black holes (e.g. Silk & Srednicki 1984, Rudaz & Stecker 1988, Kiraly et al. 1981). A particular feature of secondary antiproton production in proton-proton collisions is the kinematics of the reaction that result in a production threshold. A proton flux of the form $dn/dE = A \times E^{-2.7}$ where E is the proton kinetic energy and n the number of protons per unit time, solid angle and energy, will produce a ratio that increases rapidly as a function of energy E up to about 5 GeV.

Meanwhile, a number of experiments were performed in the energy range starting at a few hundred MeV up to about 3 GeV that confirmed the secondary antiproton production hypothesis (Mitchell et al. 1996, Moiseev et al. 1996). The major difficulty in measuring the antimatter flux is the positive identification of the rare antimatter particles in the presence of a large background. In the case of antiprotons the background is mostly electrons and, for experiments performed with balloons at small atmospheric depths, secondary pions and

4

muons that are both produced in interaction with the atmosphere.

To improve the detection efficiencies and identification of the desired and rejection of the unwanted particles, the CAPRICE experiment used a combination of an electromagnetic calorimeter and a newly developed Ring Imaging Cherenkov detector with the NMSU-WiZard/CAPRICE magnetic spectrometer. In the first CAPRICE experiment the RICH detector utilized a solid radiator of NaF, ideal for identification of antiprotons in the energy range 1-3 GeV. The CAPRICE results on positrons have been published (Barbiellini et al. 1996b). In this paper we present the CAPRICE results on antiprotons from the 1994 experiment.

Section 2 describes the experimental apparatus, section 3 the data analysis. The paper ends with a discussion in section 4.

2. Detector system

Figure 1 shows the NMSU-WiZard/CAPRICE spectrometer that was flown by balloon from Lynn Lake, Manitoba, Canada (56.5° North Latitude, 101.0° West Longitude), on 8-9 August 1994 at an atmospheric pressure of 3.2 to 4.5 mbar (altitude of 36.0 - 38.1 km) for 23 hours. It included from top to bottom: a Ring Imaging Cherenkov (RICH) detector, a time-of-flight (ToF) system, a magnet spectrometer equipped with multiwire proportional chambers (MWPC) and drift chambers (DC) and a silicon-tungsten imaging calorimeter. In the CAPRICE experiment, particular emphasis was put on particle identification. The aim was to be able to safely reject protons against positrons (Barbiellini et al. 1996b) and e^-, μ^- and π^- against $\bar{p}$ (this paper).

The 50×50 cm^2 RICH detector (Carlson et al. 1994, Barbiellini et al. 1996a), with a threshold Lorentz factor of 1.5, used a solid NaF radiator and a photosensitive MWPC

with pad readout to detect the Cherenkov light image and hence measure the velocity of the particles. The time-of-flight system had two layers, each layer made of two 25×50 cm^2 paddles of plastic scintillator, one above and one below the tracking stack. Each paddle was equipped with two 5 cm diameter photomultiplier tubes. The ToF system was used to give a trigger and to measure the time-of-flight and ionization (dE/dX) losses of the particles. The spectrometer was equipped with a superconducting magnet and multiwire proportional chambers and drift chambers (Golden et al. 1978, Golden et al. 1991, Hof et al. 1994). The magnet was 61 cm in diameter and produced an inhomogeneous field of ~ 4 T at the centre of the coil operating at a current of 120 A. The spectrometer provided 19 position measurements (12 DC and 7 MWPC) in the bending direction (x) and 12 measurements (8 DC and 4 MWPC) in the non-bending direction (y). Using the position information along with the map of the magnetic field, the rigidity of the particle was determined. The average maximum detectable rigidity was 170 GV/c.

Finally, the electromagnetic calorimeter (Bocciolini et al. 1996) consisted of eight 48×48 cm^2 silicon planes, giving both x- and y-coordinate readout. Each silicon plane was interleaved with a one radiation length thick layer of tungsten converter. The segmentation of the silicon planes into strips provided information on the longitudinal and lateral profile of the cascade along with the total energy deposit.

3. Data analysis

The analysis was based on 18 hours of data collection for a total acquisition time of 60520 seconds under an average residual atmosphere of 3.9 g/cm^2.

The data analysis must use the information available from the different detectors to safely identify the antiprotons in a very large background of other particles. Albedo

particles, as well as the large number of protons and electrons, must be rejected in the antiproton analysis. About 4% of the cosmic ray protons interact in the atmosphere above the spectrometer and produce π^- and μ^- that must be rejected. Interactions in the spectrometer and associated bar structure also results in a background of negatively charged particles. The remaining background in the antiproton sample is carefully estimated using experimental data and simulations. The selection of protons is more straightforward with little background to reject.

Based on the ability of the RICH to reliably identify antiprotons from pions, muons and electrons, the rigidity range chosen for our analysis was 1.2 to 4.0 GV/c. This rigidity range was divided into two bins: 1.2 to 2.8 GV/c and 2.8 to 4.0 GV/c. At 1.2 GV/c the RICH (anti)proton selection efficiency becomes higher than 50%. At a rigidity of 2.8 GV/c, the Cherenkov angle of (anti)protons becomes less than six standard deviations away from the Cherenkov angle of the β (velocity) ~ 1 particles (pions, muons and electrons). 4 GV/c is the rigidity where the (anti)proton Cherenkov angle becomes less than three standard deviations away from the Cherenkov angle of $\beta \sim 1$ particles.

3.1. Antiproton and proton selection

3.1.1. Albedo particles

Downgoing particles were selected using the time-of-flight information. The time-of-flight resolution of 280 ps, compared with the time-of-flight of more than 4 ns, assures that no contamination from albedo particles remains in the selected sample. This is verified by the RICH where no Cherenkov light is detected for albedo particles. The RICH was capable of rejecting $(98.1 \pm 0.5)\%$ of the albedo particles that had a high enough velocity to produce Cherenkov light in the NaF radiator.

3.1.2. Tracking

The tracking information must be carefully used to eliminate positively charged particles (protons), that have scattered in the tracking system and therefore look like negatively charged particles. Events with more than one track also must be eliminated. To achieve this goal, a set of conditions were imposed on the fitted tracks. These conditions represent a compromise between rejection power and efficiency and are partly based on experience gained previously using the same tracking system (Mitchell J. et al. 1996, Hof M. et al. 1996). They were the following:

1. At least 11 (out of 19) position measurements in the x direction and 7 (out of 12) in the y direction were used in the fit.

2. The chi-squares divided by the number of degrees of freedom for the track fit should be ≤ 4 for the x direction and ≤ 8 for the y direction.

3. The estimated error on the deflection should be < 0.04 $(GV/c)^{-1}$.

4. Not more than 3 DC layers were allowed to have additional hits at a distance larger than 4 cm from the fitted track.

5. The measured deflections using the upper and lower halves of the spectrometer should agree with those using the complete spectrometer.

Criterion 4 was introduced to reject multiple track events and criterion 5 to eliminate events in which a hard scattering had occurred. Visual inspection showed that all events rejected by criterion 4 had multiple tracks coming from above. No events with interactions in the calorimeter were rejected by this condition.

3.1.3. Scintillators

Particles with charge one were selected using the measured energy loss in the top scintillator. From the observed distribution of the dE/dX as a function of rigidity, singly charged proton like events were selected in the following manner. An upper cut on the dE/dX was made, which corresponds to the most probable energy loss by a proton plus 0.8 times the energy loss by a minimum ionizing particle. This criterion eliminates events where the (anti)proton was accompanied by a second particle. A lower cut was set below the most probable dE/dX for protons by three times the observed energy loss resolution. Multiple charged tracks produced in interactions above the tracking system were rejected by requiring that not more than one of the two paddles be hit in the top scintillator plane. We chose not to impose any conditions on the bottom scintillators to avoid losing events where an interaction in the calorimeter could produce back scattered particles which traverse the bottom scintillator paddles.

3.1.4. RICH

The RICH was used to measure the Cherenkov angle of the particle and thereby its velocity. The velocity and incidence angle dependent Cherenkov angle resolution were determined using a large number of protons selected by the calorimeter and the scintillators. The resolution varied from 8 mrad (perpendicular incidence and $\beta \sim 1$) to about 23 mrad (10° off perpendicular incidence and $\beta = 0.78$). Since the RICH is the only detector capable of clearly identifying antiprotons against a background of muons, pions and electrons in the rigidity range 1.2 to 4 GV/c, strict cuts were applied on the RICH data:

1. A good agreement between the particle's impact position as determined by the RICH and the tracking system was required. The difference in x and y should be less than

three standard deviations (rigidity dependent), typically < 5 mm.

2. Cuts on the number of pads (proportional to the number of detected Cherenkov photons) used for the reconstruction of the Cherenkov angle were also applied. More than 8 pads were required in the fit.

3. Charged particles produce significantly higher signals than Cherenkov photons do in the pads. This was used to reject events with multiple charged tracks traversing the RICH, by requiring that there was only one cluster of pads with high signals.

4. The reconstructed Cherenkov angle should not deviate by more than three standard deviations from the expected Cherenkov angle for (anti)protons.

5. To suppress the background from lighter particles, the reconstructed Cherenkov angle was required to be more than three standard deviations (30 mrad) away from the expected Cherenkov angle for pions (the heaviest background particle).

Using these conditions, reliable Cherenkov angle information was obtained. Figure 2 shows the Cherenkov angle as a function of rigidity for positive and negative particles. One can clearly identify the different particle types. The squares show the Cherenkov angle of the identified antiprotons after all cuts have been applied.

3.1.5. Calorimeter

The calorimeter was used to identify electromagnetic showers. The longitudinal and transverse segmentation of the calorimeter combined with the measurement of the energy lost by the particle in each silicon strip resulted in high identification power ($\sim 85\%$) for electromagnetic showers combined with a high rejection power ($\sim 10^4$) for hadronic particles (Barbiellini et al. 1996). In the analysis presented in this paper, the calorimeter was

used to reject events with electromagnetic showers initiated by a single electron, possibly accompanied by a bremsstrahlung photon emitted in the RICH or in the dome above the detector stack (see Weber 1997 for a description of the selection criteria).

Figures 3 and 4 illustrate the calorimeter performance, and show schematic views of two single events in the CAPRICE apparatus. The instrument is shown in the bending (x) view and in the non-bending (y) view. From top to bottom is displayed: the RICH seen from above, the tracking stack of multiwire proportional chambers and drift chambers, and the imaging calorimeter. Note that Figures 3 and 4 are not to scale; the calorimeter is significantly thinner than shown in the figure. Figure 3 shows a single 1.3 GV/c electron traversing the apparatus and emitting a bremsstrahlung photon in the RICH. The RICH shows the detected Cherenkov light image where the ionization of the chamber gas by the electron is shown as a cluster of pads hit in the centre surrounded by the signals from the Cherenkov light. Due to total reflection in the NaF crystals, only part of the Cherenkov ring is detected. The tracking stack shows the trajectory of the electron as it is deflected by the strong magnetic field. The calorimeter shows the two electromagnetic showers produced by the electron and the bremsstrahlung photon, respectively. The origin of the bremsstrahlung photon can be located by projecting backward the direction of the shower and determining where it intersects the electron trajectory. More than one fourth of the electrons in the rigidity region 1.2 to 4 GV/c were accompanied by a bremsstrahlung photon reconstructed in the calorimeter.

Similarly, Figure 4 shows a single 2.2 GV/c antiproton traversing the instrument. The ring of Cherenkov light is clearly seen in the RICH, giving an accurate velocity determination for the particle. The rigidity is measured from the deflection in the tracking system. The antiproton interacts in the calorimeter, clearly showing many charged particles emerging from the vertex of interaction; this could be an in-flight annihilation. The

interaction probability for a 2.2 GV/c antiproton is about 40%.

3.1.6. The bar

A 17 kg, 1.2 m long aluminium bar with a 7 kg steel hook in the centre, used to connect the payload to the balloon, was situated 2.3 m above the RICH. The production and loss of particles in the non-uniform I-shaped bar cannot be estimated reliably and hence we chose to reject all particles crossing it. This was done by extrapolating the tracks to the level of the bar. This cut results in a 10% reduction of the geometrical factor.

3.2. Selection results

Nine antiprotons were found in the flight data after applying the selection criteria described above (see Table 3). Of the nine antiprotons, two (one in the first bin and one in the second) were found to have interacted in the calorimeter. This is in agreement with the simulated expectation of 3.4 ± 1.1 antiproton interactions in the calorimeter. One should note that not all antiproton interactions give a detectable signal in the calorimeter.

3.3. Efficiency

Whereas protons and antiprotons have very similar efficiencies in the RICH, scintillators, and the tracking system, this is not the case for the calorimeter due to the large difference in interaction properties.

A large proton sample of about 100000 events from the flight data, was used to determine the RICH, scintillator and tracking efficiencies as a function of rigidity. Simulations were used to determine the calorimeter efficiency for antiprotons. The resulting

efficiencies are shown in Figure 5 and are given in Table 1.

The scintillator efficiency was high and, as expected, only weakly dependent on the rigidity. The tracking efficiency was slightly under 70% and includes the contributions from the individual chamber efficiencies, δ-ray production, scattering, etc..

The RICH efficiency was strongly rigidity dependent. The sharp increase with rigidity above 1 GV/c was due to the increasing number of Cherenkov photons emitted, and hence an increased number of pads with a detectable signal. The decrease of the RICH efficiency above 2.5 GV/c is caused by the requirement that the Cherenkov angle should be more than 30 mrad away from the expected Cherenkov angle for pions.

The calorimeter was mainly used to reject electrons, which are the main background in the antiproton selection. The antiproton efficiency of the calorimeter was obtained from a Monte Carlo simulation based on the CERN GEANT/FLUKA-3.21 code (Brun et al. 1994). In the simulation, the full spectrometer including the magnetic field was used. The simulation results were compared with the results from beam tests of the calorimeter and a good agreement was found (Bocciolini et al. 1993). The simulations show that the calorimeter detection efficiency for antiprotons is rigidity dependent, as shown in Figure 5 and Table 1.

For the proton selection the same criteria as for the antiprotons were used. The detection efficiencies are the same except for the calorimeter which, from an experimental proton sample, selected by RICH, dE/dX and time-of-flight, was found to be $(99.21 \pm 0.03)\%$ efficient and independent of rigidity.

3.4. Contamination

The contamination due to e^-, μ^- and π^- in the antiproton sample was carefully studied using the two independent detectors: the RICH and the calorimeter. Simulations and experimental data taken during the flight and in ground before the flight were used.

The calorimeter was particularly well suited to reject electrons. Detailed simulation studies showed that the shower reconstruction algorithm, designed to reject electrons while keeping as large a fraction as possible of the antiprotons, rejected 97.4% of the electrons nearly independent of rigidity in the interval 1.2-4 GV/c, leaving 2.6% as background. In principle, the calorimeter cuts could have a larger electron rejection power but, due to the low antiproton statistics, we chose to use calorimeter selection criteria with large efficiency even if the electron contamination is not minimized. However, the use of the RICH as the main detector to distinguish antiprotons from light particles ensures a low level of background.

The electron contamination in the RICH was studied using a sample of 1323 e^- in the interval 1.2 to 4 GV/c, selected using the calorimeter and dE/dX in the scintillators. Of the 1323 events, two out of 1052 were accepted as $\bar{p}$ in the rigidity range 1.2 to 2.8 GV/c, and two out of 271 in the rigidity range 2.8 to 4 GV/c. As expected, the RICH rejection power was rigidity dependent. The surviving fraction of electrons increased from $(0.2 \pm 0.1)\%$ between 1.2 and 2.8 GV/c to $(0.7 \pm 0.5)\%$ between 2.8 and 4 GV/c.

The combination of the calorimeter and the RICH resulted in a very small background from electrons (and interacting pions) in the antiproton sample. The electron (and interacting pion) contamination was determined by selecting all non-minimum ionizing particles in the calorimeter (1388 events, mainly e^- and a few interacting π^- and $\bar{p}$) in the rigidity range 1.2 to 4 GV/c. A non-minimum ionizing particle is defined as a particle which deposits more energy in the calorimeter than a minimum ionizing particle (see Weber

14

1997). Multiplying this number by the electron rejection factors of the RICH and the calorimeter resulted in a contamination in the whole antiproton sample of less than 0.15 electrons (and interacting pions), see Table 2.

Tests in particle beams showed that muons and electrons have the same detection efficiency in the RICH. Therefore, it was assumed that the surviving fraction of muons was equal to the surviving fraction of electrons. This was also checked using ground data. Before the flight, long ground runs were performed where more than 400000 events were collected. The tracking, dE/dX and calorimeter (anti)proton selection criteria resulted in 12819 events with negative curvature in the rigidity range 1.2 to 4 GV/c (mainly muons). The RICH (anti)proton selection criteria were applied to these events resulting in contamination values in good agreement with the values obtained for the electrons from flight data. The surviving fraction of muons was found to be $(0.23 \pm 0.05)\%$ in the first bin and $(0.68 \pm 0.13)\%$ in the second. These numbers were used to define the contamination from the negative muons and non-interacting pions.

Defining negative muons (and non-interacting pions) as events with a minimum ionizing behaviour in the calorimeter, 387 and 99 muons and pions were selected from the flight data between 1.2 and 2.8 GV/c, and 2.8 and 4 GV/c, respectively. Multiplying these numbers with the surviving fraction numbers found above, the muon/pion contamination was found to be 0.9 ± 0.2 muons/pions in the first energy bin and 0.7 ± 0.1 in the second bin. This contamination, and the small electron and non-interacting pion contamination, was later subtracted from the antiproton signal and is shown in parenthesis in Table 3. It is worth noting that the calorimeter cannot separate muons and pions from non-interacting antiprotons and therefore cannot be used to further reject muons and pions.

As a cross check, the calorimeter electron rejection criteria were applied on all negative events leaving 433 particles (muons, pions, antiprotons and 2.6% of the electrons) between

15

1.2 and 2.8 GV/c, and 118 events between 2.8 and 4 GV/c. Multiplying these numbers with the RICH rejection power determined for the ground muons results in a contamination of 1.0 ± 0.2 in the first bin, and 0.8 ± 0.2 in the second. This is in agreement with the previous results. The background analysis results are summarized in Table 2.

3.5. Antiproton flux and antiproton to proton ratio at the top of the atmosphere

To obtain the antiproton flux and the antiproton to proton ratio at the top of the atmosphere, it is necessary to correct for the number of secondary particles produced and lost in the residual atmosphere and in the instrument itself. Furthermore, the detector efficiencies, geometrical factor and total live time have to be taken into account.

The geometrical factor (G) at different rigidities was obtained with a Monte Carlo technique (Sullivan 1971), see Table 4. The fractional dead time during the flight was 0.7310 ± 0.0006 resulting in a total live time (T_{live}) of 16280 ± 36 s.

Since the detector efficiencies varied with rigidity, it was important to properly define the rigidity values at which these efficiencies had to be estimated. For protons, the rigidity range was split into bins of 50 MV/c width, narrow enough that the efficiencies do not vary appreciably inside each bin. For each bin we counted the number of protons and corrected for the detector efficiency. For the antiprotons, because of the low statistics, the efficiencies were weighted with a theoretical antiproton flux (see Table 1). In this process we used the expressions for the mean interstellar antiproton flux given by Gaisser and Schaefer (1992), corrected for the solar modulation conditions during the CAPRICE flight. The solar modulated flux (Flux_{mod}) at an energy E is given as function of the interstellar flux

(Flux) by (Gleeson and Axford 1968):

$$\text{Flux}_{mod}(E) \; = \; \frac{E^2 + 2\,m_0\,E}{(E + Ze\Phi)^2 + 2\,m_0\,(E + Ze\Phi)}\,\text{Flux}(E + Ze\Phi)$$

where E is the kinetic energy in MeV, Ze the charge of the particle and m_0 the (anti)proton rest mass. The parameter Φ for the CAPRICE flight was found to be 500 MV using data from the neutron monitor counter CLIMAX (Chicago 1996) and the work by Paradis (1995).

All antiprotons and protons interacting with the payload material above the tracking system were assumed to be rejected by the selection criteria. The data were corrected for these losses with multiplicative factors, using the expression for the interaction mean free path for the different materials in the detectors given by Stephens (1996). The corrected number of antiprotons and protons at the top of the payload are given in Table 3.

The production of secondary antiprotons in the atmosphere has been studied by several authors (Pfeifer et al. 1996, Stephens 1996). For the atmospheric secondary antiproton production, we used the calculation by Stephens (1996) and for that of protons the data of Papini et al. (1996). The secondary produced particles were normalized with the acceptance and live time of the experiment, and subtracted from the corrected numbers using a mean residual atmosphere of 3.9 g/cm^2. Finally, the data were corrected for losses in the atmosphere above the detector due to interactions, giving the number of antiprotons $(N_{\bar{p}}^{TOA})$ and protons (N_p^{TOA}) at the top of the atmosphere, see Table 3.

The antiproton flux is given by

$$\text{Flux(E)} \; = \; \frac{1}{T_{live} \times G \times \Delta E} \times N_{\bar{p}}^{TOA}(E)$$

where ΔE is the energy bin corrected to the top of the atmosphere. The resulting antiproton flux is given in Table 4. The total errors include both statistical and systematic errors. Figure 6 shows the antiproton flux at the top of the atmosphere measured by this and other

17

recent experiments together with theoretical predictions. The theoretical antiproton limits were set by Gaisser and Schaefer (1992), assuming that the source of interstellar antiprotons is interaction of cosmic rays with the interstellar medium. The theoretical fluxes, but not the experimental values of the other experiments, were corrected for the solar modulation conditions corresponding to the CAPRICE flight (Φ).

The antiproton to proton ratio was calculated from

$$R(E) = N_{\bar{p}}^{TOA}(E)/N_p^{TOA}(E)$$

and is summarized in Table 3. The ratio is also presented in Figure 7 along with the results from other balloon experiments and theoretical predictions by Gaisser and Schaefer (1992).

4. Discussion

For the first time, the combination of an electromagnetic calorimeter and a ring imaging Cherenkov detector has been used to measure the cosmic ray flux of antiprotons. This combination has made it possible to accurately identify antiprotons in the presence of a large background of lighter, negatively charge particles. It also allows an accurate determination of the contamination within the antiproton sample.

The flux of antiprotons and the ratio of antiprotons to protons increase over the kinetic energy interval 0.6 to 3.2 GeV. In agreement with other recent data (e.g. Mitchell et al. 1996), it supports the conjecture that the antiprotons in this energy range are produced in the interstellar medium by primary cosmic rays colliding with interstellar gas.

The combination of all available data on the ratio in the energy range 0.3 to 3 GeV (Moiseev et al. 1996, Bogomolov et al. 1987 & 1990, Mitchell et al. 1996, and this work), shows an increase with energy in agreement with calculations by Gaisser and Schaefer (1992). However, the combined data do not rule out a faster increase than calculated. The

18

two measurements that have been reported above 4 GeV by Golden et al. (1984) and by the MASS91 experiment (Hof et al. 1996) differ by about three standard deviations and further measurements are clearly needed in order to rule out any exotic antiproton production. Fortunately, new experiments are in progress.

For very low kinetic energies, below 0.5 GeV, the solar modulation affects the flux significantly. However, the existing data do not rule out contributions from, for example, dark matter particle annihilations. Calculations by Mitsui et al. (1996) show that in the above scenario the antiproton spectrum would flatten at lower energies; new experiments are in progress to test this scenario. A flattening at low energies could also be caused by diffuse scattering on hydromagnetic waves, as shown by Simon et al. (1996).

New experimental facilities will soon become available with space borne magnetic spectrometers (e.g. Adriani et al. 1995) that will allow long exposure times and thereby give statistically improved data on the antiproton flux.

Table 1. Antiproton selection efficiencies.

Rigidity at the spectrometer GV/c	Tracking efficiency %	dE/dX top scintillator efficiency %	RICH efficiency %	Calorimeter efficiency %
1.2 - 2.8	67.6 ± 0.4	96.5 ± 0.2	70.2 ± 1.0	93.9 ± 0.4
2.8 - 4.0	68.6 ± 0.5	94.7 ± 0.2	45.3 ± 1.0	97.7 ± 0.3

Table 2. Muon and electron contamination.

Rigidity at the spectrometer GV/c	Electrons		Muons and pions	
	before RICH and calorimeter selection	Expected number of misidentified $\bar{p}$	before RICH and calorimeter selection	Expected number of misidentified $\bar{p}$
1.2 - 2.8	1098	0.07 ± 0.02	387	0.9 ± 0.2
2.8 - 4.0	290	0.06 ± 0.01	99	0.7 ± 0.1

Table 3. Summary of proton - antiproton results.

Rigidity at spectrometer GV/c	Observed number of events[a]		Extrapolated number at top of payload		Atmospheric correction		$\frac{\overline{p}}{p}$ at TOA[b]
	$\overline{p}$	p	$\overline{p}$	p	$\overline{p}$	p	
1.2 - 2.8	4(1)	124658	8.6	303433	1.5	8484	2.5 $(+3.2,-1.9) \times 10^{-5}$
2.8 - 4.0	5(0.7)	25260	17.7	90451	1.4	1662	1.9 $(+1.6, -1.0) \times 10^{-4}$

[a]The numbers shown in the brackets are the estimated muon, pion and electron background.

[b]Top of the Atmosphere. The quoted errors are a combination of statistical and systematic errors.

Table 4. Antiproton and proton fluxes at the top of the atmosphere.

Kinetic Energy at TOA[a] GeV	Geometrical factor $(m^2\ sr)^{-1}$	Antiproton flux at TOA[b] $(m^2\ sr\ s\ GeV)^{-1}$	Proton flux at TOA[b] $(m^2\ sr\ s\ GeV)^{-1}$
0.6 - 2.0	179.1 ± 2.8	$1.9\ (+2.4, -1.4) \times 10^{-2}$	743 ± 17
2.0 - 3.2	177.5 ± 2.8	$5.3\ (+4.5, -2.9) \times 10^{-2}$	278 ± 10

[a]Top of the Atmosphere.

[b]The quoted errors are a combination of statistical and systematic errors.
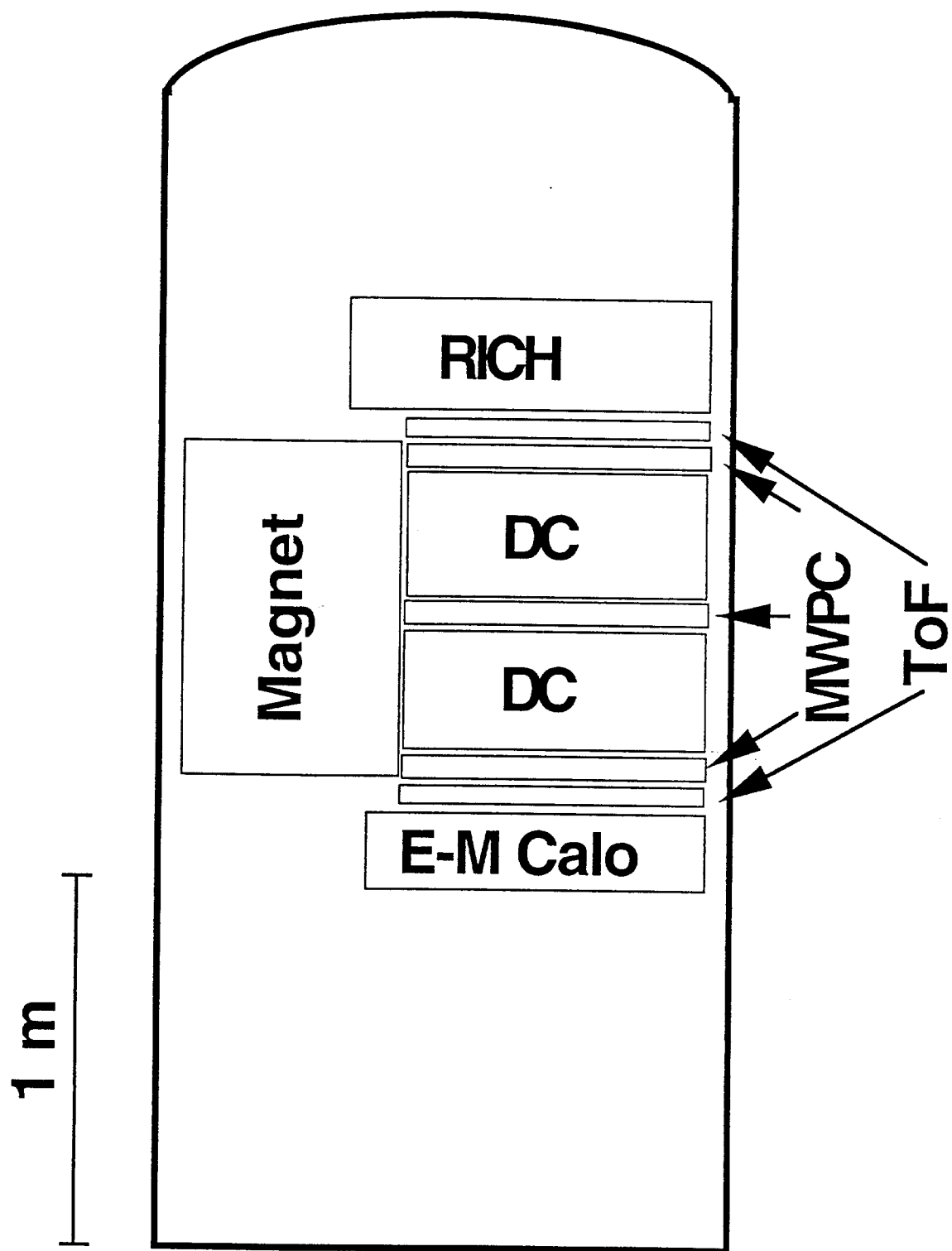
Fig. 1.— Schematic view of the CAPRICE apparatus.
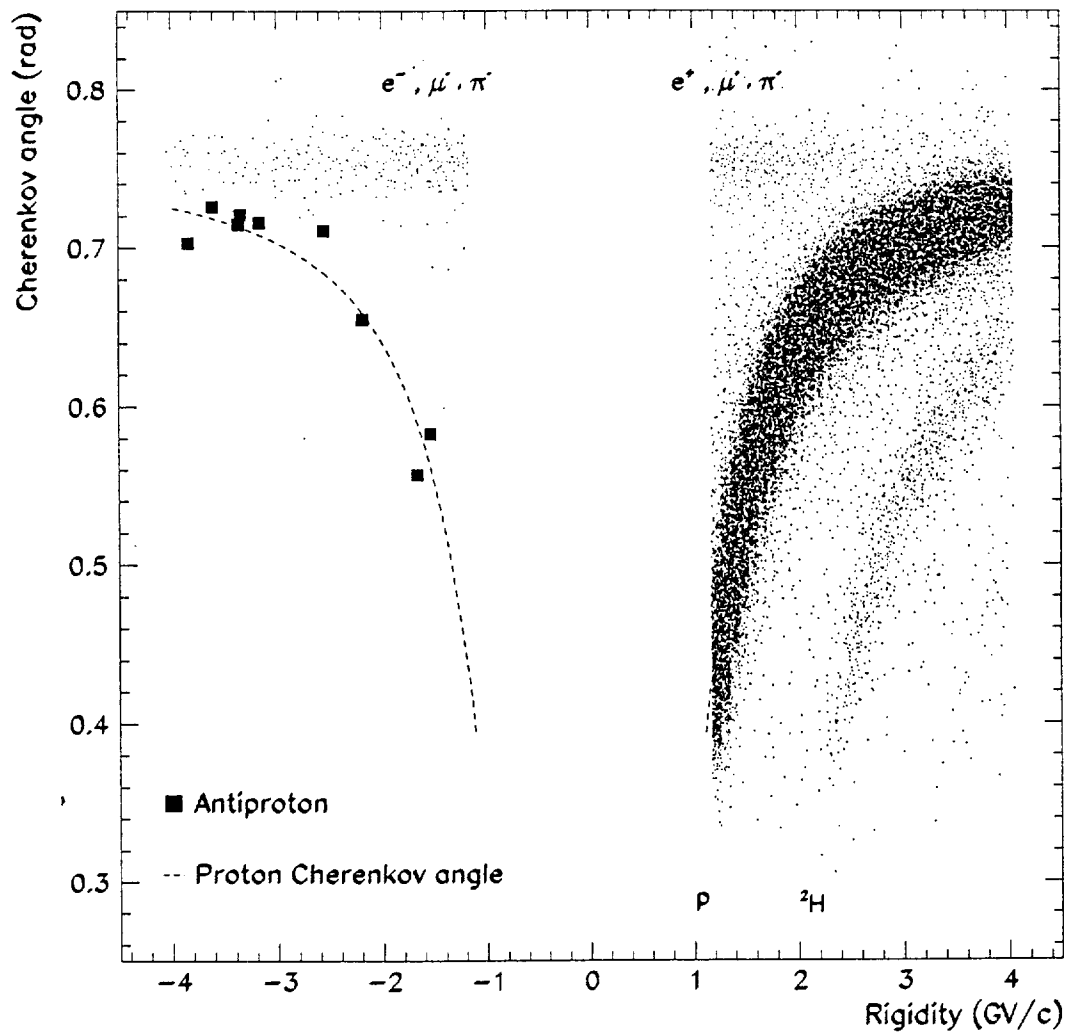
Fig. 2.— Scatter plot of the Cherenkov angle versus rigidity for negative and positive particles after tracking, dE/dX and calorimeter antiproton selection. 404 negative and ~ 160000 positive (~ 150000 protons) events are selected in the rigidity range 1.2 to 4 GV/c. The squares show the selected antiprotons.
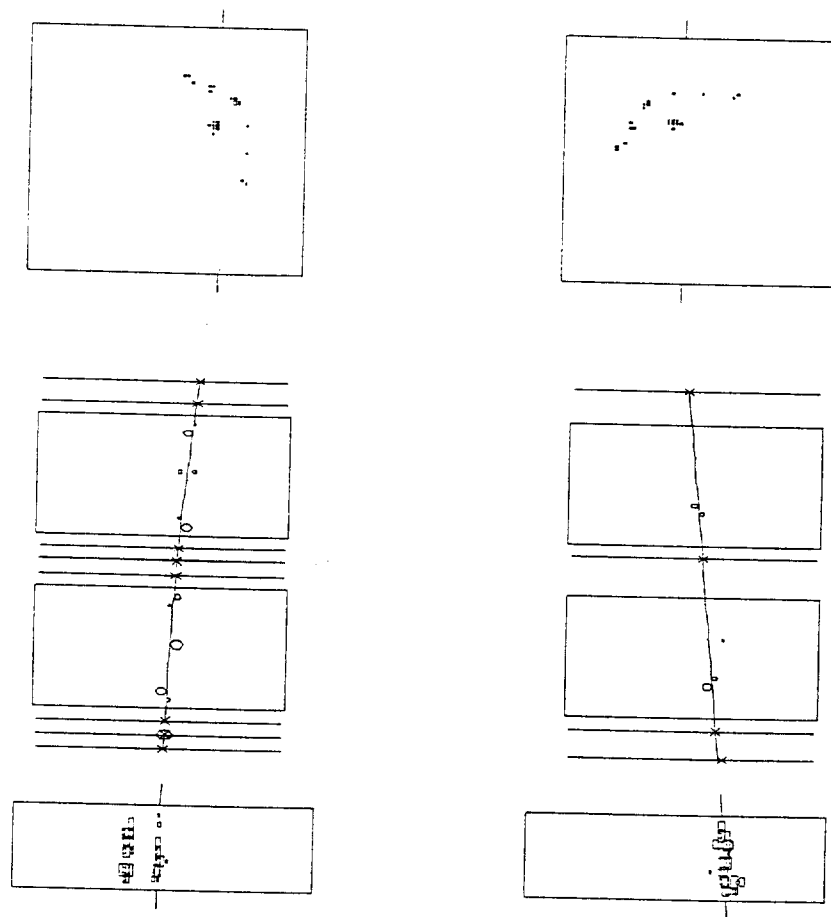
Fig. 3.— Display of a single 1.3 GV/c electron in the CAPRICE apparatus. The electron emits, according to an extrapolation of the track, a bremsstrahlung photon in the RICH. The instrument is shown in the bending (x) view (left) and in the non-bending (y) view (right). From top to bottom is displayed: the RICH seen from above, the tracking stack of multiwire proportional chambers and drift chambers, and at the bottom the imaging calorimeter. Crosses indicate hits in the MWPC and circles in the DC with the radius proportional to the drift time. Note that the figure is not scaled. The calorimeter is significantly thinner than shown in the figure. The calorimeter shows the two electromagnetic showers produced by the electron and by the bremsstrahlung photon, respectively. In the non-bending view the two showers overlap.
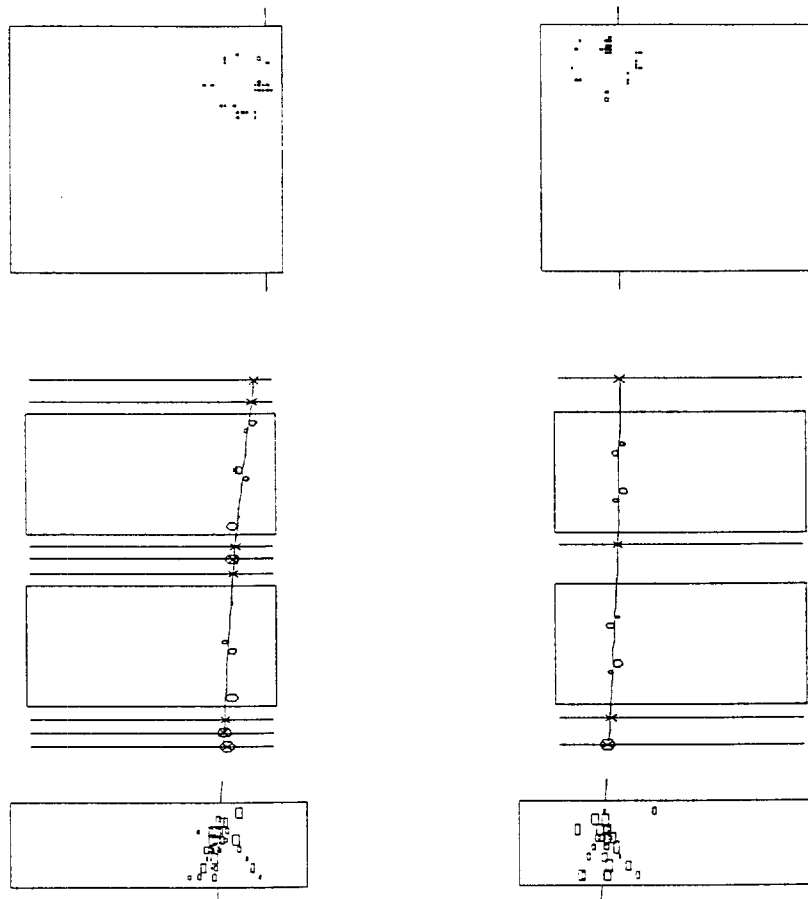
Fig. 4.— Display as in figure 3 of a single 2.2 GV/c antiproton traversing the CAPRICE apparatus. The antiproton interacts in the calorimeter showing clearly several charged particles emerging from the vertex of interaction; this could be an annihilation in flight.
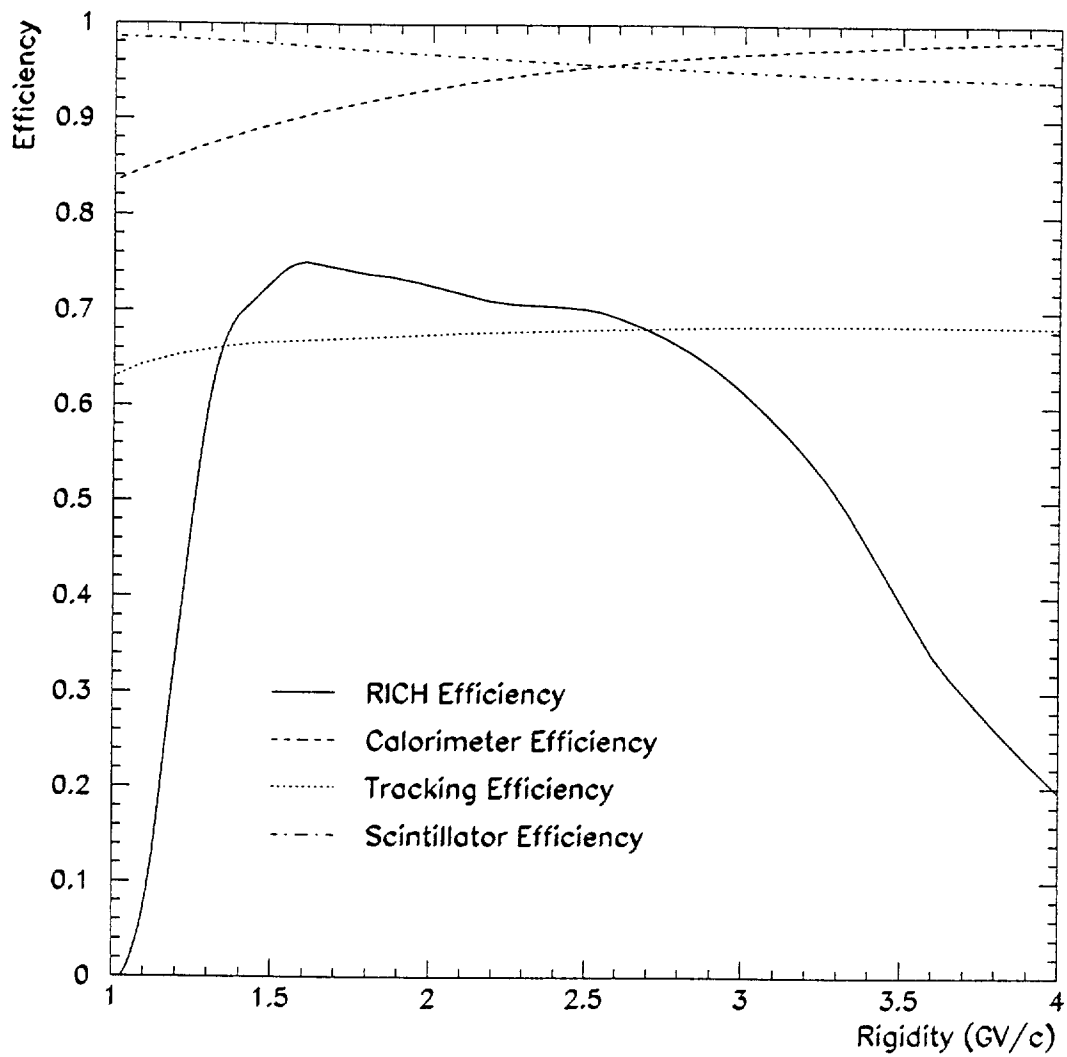
26

Fig. 5.— Efficiencies for the different parts of the spectrometer for detecting antiprotons. Determined from data are the efficiencies of the RICH (solid line), the tracking system (dotted line) and the scintillator dE/dX cut (dashed-dotted line). The efficiency of the calorimeter antiproton cuts (dashed line) was determined by simulation.
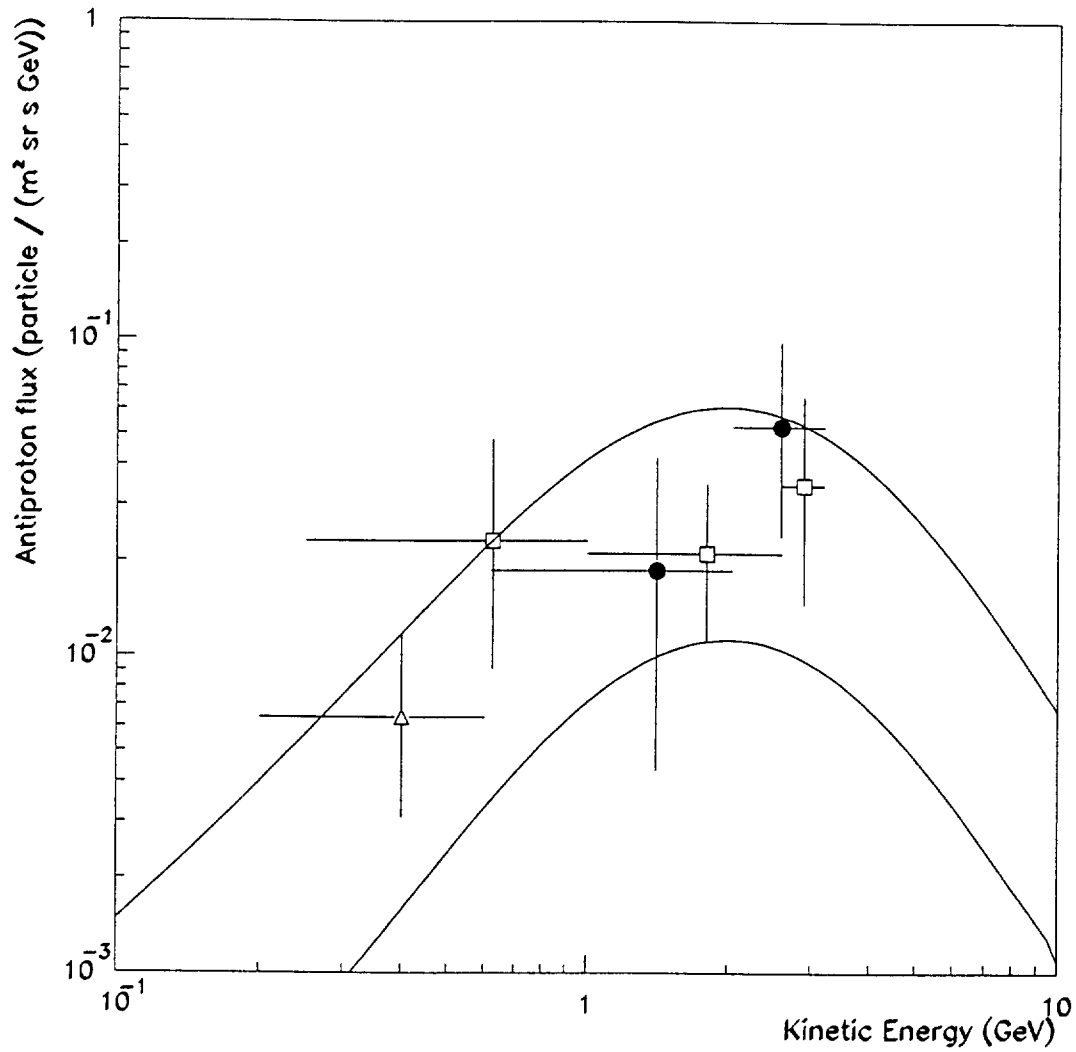
Fig. 6.— The antiproton flux at the top of the atmosphere obtained in this work and compared to other recent experiments that has published results on the antiproton flux. Data from Mitchell et al 1996 (open box), Moiseev et al. 1996 (open triangle) and this work (filled circle). The solid lines are the maximum and minimum $\bar{p}$ fluxes as calculated by Gaisser & Shaeffer (1992). The theoretical fluxes, but not the experimental values, were corrected for the solar conditions during the CAPRICE flight.
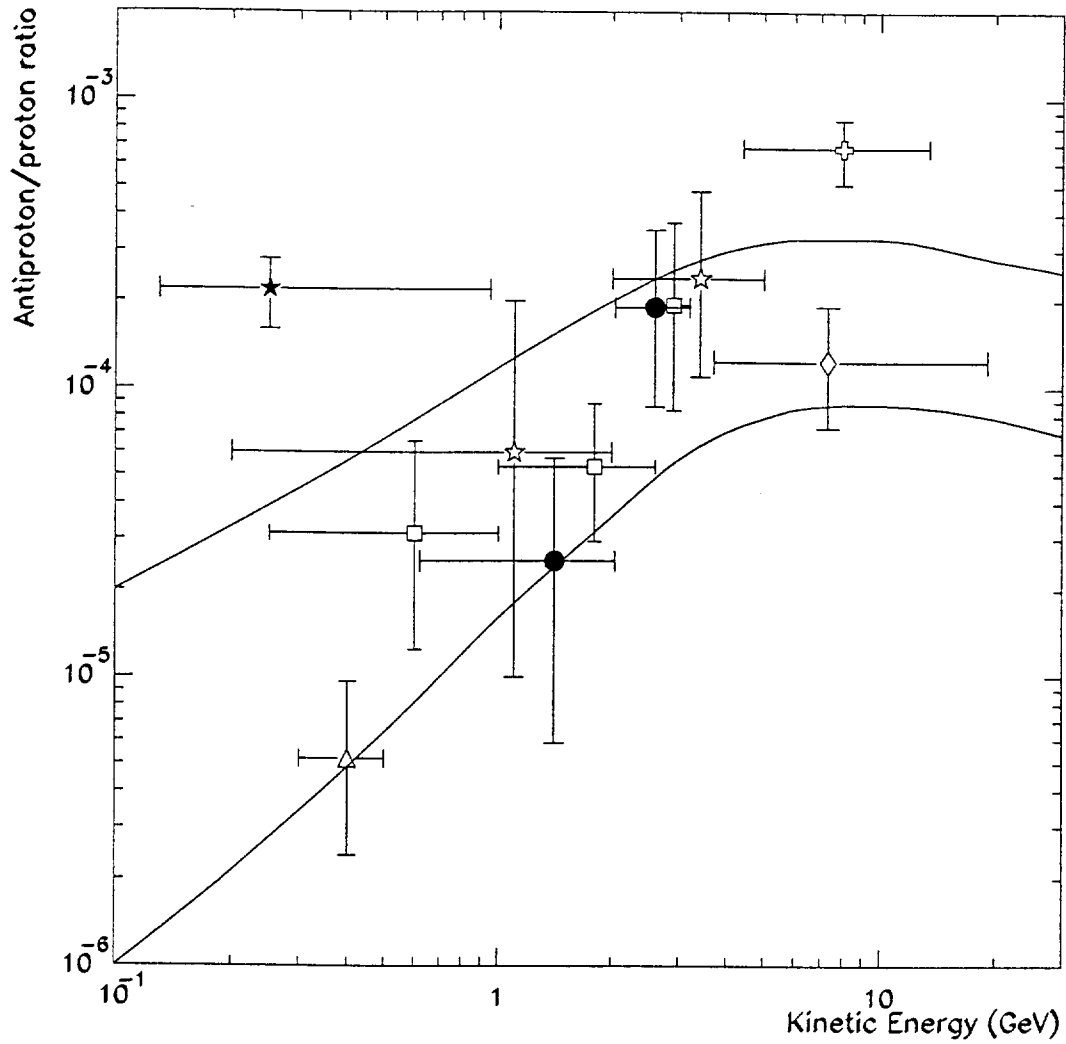
Fig. 7.— The $\bar{p}$ /p ratios at the top of the atmosphere obtained in this work compared with previous measurements. Data from Golden et al. 1984 (open cross), Buffington et al. 1981 (filled star), Bogomolov et al. 1987 & 1990 (open star), Mitchell et al 1996 (open box), Hof et al. 1996 (open diamond), Moiseev et al. 1996 (open triangle) and this work (filled circle). Experiments reporting only upper limits have been omitted. The solid lines are the maximum and minimum ratios as calculated by Gaisser & Shaeffer (1992).

29

REFERENCES

Adriani, O., et al. 1995, Proc. of XXIV ICRC, Rome, 3, 591

Barbiellini, G., et al. 1996a, Nucl. Instr. and Meth., A371, 169

Barbiellini, G., et al. 1996b, A&A, 309, L15

Bocciolini, M., et al. 1993, Nucl. Instr. and Meth., A333, 77

Bocciolini, M., et al. 1996, Nucl. Instr. and Meth., A370, 403

Bogomolov, E. A. et al. 1979, Proc. of XVI ICRC, Kyoto, 1, 330

Bogomolov, E. A. et al. 1987, Proc. of XX ICRC, Moscow, 2, 72

Bogomolov, E. A. et al. 1990, Proc. of XX1 ICRC, Adelaide, 3, 288

Brun, R., et al. 1994, "Detector Description and Simulation Tool", CERN program library

Buffington, A., Schindler, S. M., & Pennypacker, C. R. 1981, ApJ, 248, 1179

Carlson, P., et al. 1994, Nucl. Instr. and Meth., A349, 577

University of Chicago 1996, National Science Foundation Grant ATM-9420790,
     http://astro.uchicago.edu/home/web/pyle/neutron.html

Gaisser, T. K., & Schaeffer, R. K. 1992, ApJ, 394, 174

Gleeson, L. J., & Axford, W. I. 1968, ApJ, 154, 1011

Golden, R. L., et al. 1978, Nucl. Instr. and Meth., 148, 179

Golden, R. L., et al. 1979, Phys. Rev. Lett., 43, 1264

Golden, R. L., et al. 1984, Astrophys. Lett., 24, 75

Golden, R. L., et al. 1991, Nucl. Instr. and Meth., A306, 366

Hof, M., et al. 1994, Nucl. Instr. and Meth., A345, 561

Hof, M., et al. 1996, ApJ, 467, L33

Kiraly, P., Wdowczyk, J., & Wolfendale, A. 1981, Nature, 293, 120

Mitchell, J., et al. 1996, Phys. Rev. Lett., 76, 3057

Mitsui, T., Maki, K., & Orito, S. 1996, "Expected Enhancement of the Primary Antiproton
    Flux at the Solar Minimum", UT-ICEPP 96-03, 22

Moiseev, A., et al. 1996, "Cosmic Ray Antiproton Flux in the Energy Range from 200 to
    600 MeV", ApJ, to appear 1997

Papini, P., Grimani, C., & Stephens, S. A. 1996, Il Nuovo Cimento, 19, 367

Paradis, P. 1996, PhD thesis, New Mexico State University, USA

Pfeifer, Ch., Roesler, S., & Simon, M. 1996, Phys. Rev. C, 54, 2, 54

Rudaz, S., & Stecker, F. W. 1988, ApJ, 325, 16

Silk, J., & Srednicki, M. 1984, Phys. Rev. Lett., 53, 624

Simon, M., et al. 1996, ApJ, 456, 519

Stecker, F. W., Protheroe, R. J., Kazanas, D. 1981, Proc. of XVII ICRC, Paris, 9, 211

Stecker, F. W. & Wolfendale, A. W. 1984, Nature, 309, 37

Stephens, S. A. 1996, "Secondary Antiproton Spectrum in the Atmosphere with the
    Inclusion of Fermi Motion in Air Nuclei", submitted to Astropart. Phys.

Sullivan, J. D. 1971, Nucl. Instr. and Meth., 95, 5

31

Weber, N. 1997, "A measurement of the antiproton and proton fluxes in the cosmic rays by the CAPRICE experiment" (PhD thesis, KTH Stockholm, Sweden)